PAPER

Check for updates

Soft-templated, mesoporous Co_3O_4 thin films for electrocatalysis of the oxygen evolution reaction†

Qingyang Wu,[a] Maximilian Mellin, [ID][a] Stefan Lauterbach,[b] Chuanmu Tian,[a] Christian Dietz, [ID][c] Jan P. Hofmann [ID][a] and Marcus Einert [ID] *[a]

In order to decrease the overpotentials required for the electrocatalytic water splitting reaction, high-performance and abundant-element based-electrocatalysts have to be developed. Especially, high-surface-area materials are considered as promising candidates to drive the oxygen evolution reaction (OER) at low overpotentials in alkaline and acidic media owing to a large amount of available active surface sites. In this context, mesoporous spinel cobalt oxide (meso-Co_3O_4) thin films on conductive substrates were prepared for the first time by the dip-coating and soft-templating approach using cobalte nitrate as precursor and commercially available, low-cost Pluronic® F-127 as structure-directing agent. By making use of the evaporation-induced self-assembly (EISA) process, citric acid was applied as structural stabilizer reported yet to be only compatible with customized polymers for formation of mesoporous thin films. The usage of commercial Pluronic® F-127 was reported to result in breakdown of the mesoporous framework. However, this work shows that both Pluronic® F-127 and citric acid are compatible and can be utilized to produce uniform mesoporous networks after annealing. The meso-Co_3O_4 thin film was found to be crack-free on the nano- and macroscale, thus offering a highly accessible nanoarchitecture ensuring a large interface to any electrolyte allowing for efficient mass transport. The surface and bulk morphology, crystallographic structure, and surface composition of the mesostructured Co_3O_4 thin film were correlated to its OER activity. The Co_3O_4 nanostructure showed, when applied as OER catalyst, a low overpotential of 340 mV *vs.* RHE at 10 mA cm^{-2} in 1 M KOH. The electrochemical performance was evaluated by means of impedance spectroscopy and Tafel plot analysis confirming enhanced electron transfer at the electrode/electrolyte interface. The Co_3O_4 electrocatalyst exhibited a promising stability under alkaline conditions over more than 4 hours upon chronopotentiometry (OER-activity loss of only 2% at 10 mA cm^{-2}). Our preparation procedure reveals the general capability of combining commercial copolymer templates with citric acid and can be transferred to other metal oxides to produce low-cost and high-surface-area materials for electrochemical applications.

Introduction

To slow down CO_2 emission and substitute fossil fuels, sustainable energy sources need to be utilized.[1,2] Electrocatalytic water splitting is a promising approach to produce hydrogen as renewable energy vector. In principle, in an electrochemical cell, the hydrogen evolution reaction (HER) occurs through reduction of protons at the cathode, and by oxidation of water, the oxygen evolution reaction (OER) is driven at the anode.[3–5] However, considerable overpotentials (η) are necessary to drive both reactions, while it is known that the OER is the efficiency-limiting process of water splitting since it requires four electrons to be transferred for the production of one molecule of O_2. In contrast, for the HER, only two electrons are involved.[6] Therefore, the exploration of high-performance, cheap and durable electrocatalysts for the OER is essential to make electrocatalytic water splitting economically competitive to already existing hydrogen production technologies (such as the steam reforming process). Noble metal oxides such as iridium oxide (IrO_2) and ruthenium oxide (RuO_2) were thoroughly examined as OER catalysts in acidic and alkaline media,[7] respectively, and have been most frequently utilized for the past decades.[8–10] However, the high cost in production

[a] *Surface Science Laboratory, Department of Materials and Earth Sciences, Technical University of Darmstadt, Otto-Berndt-Strasse 3, 64287 Darmstadt, Germany. E-mail: meinert@surface.tu-darmstadt.de*

[b] *Institute for Applied Geosciences, Geomaterial Science, Technical University of Darmstadt, Schnittspahnstrasse 9, 64287 Darmstadt, Germany*

[c] *Institute of Material Science, Physics of Surfaces, Technical University of Darmstadt, Peter-Gruenberg-Strasse 2, 64287 Darmstadt, Germany*

† Electronic supplementary information (ESI) available. See DOI: https://doi.org/10.1039/d3ma01054f

and low resources of ruthenium and iridium as elements are inevitably drawbacks for industrial up-scaling purposes. As a consequence, the search for non-noble (transition) metal-based electrocatalysts with comparable electrocatalytic performance, which are abundant, and thus low in cost, seems to be vital toward commercialisation. In this context, as early as 1987, it has been revealed that incorporating Fe into nickel oxide can significantly enhance the OER performance.[11] The NiFe-based materials offered a comparable OER performance to those of noble metal oxides, meanwhile they are more cost-efficient and abundant as elements on earth. Thus, the alloy of nickel, iron, and chromium is still to date the most utilized catalyst for water electrolysis industrial-wise.[12] However, the mechanism of their OER process still remains partially unclear and the NiFe-based nanomaterials still suffer from insufficient stability.[13]

As an alternative, cobalt-based oxides have attracted attention as electrocatalysts since cobalt is also an abundant element on earth, its oxides show good stability in aqueous electrolytes, and they have been proven to lower the OER overpotential substantially comparable to other catalytically active transition metal oxides (TMOs) such as NiO_x[14,15] or Fe_3O_4.[16] The electrocatalytically active reaction sites in spinel cobalt oxide (Co_3O_4), which are known to be mainly Co^{3+} centres, allow Co_3O_4 nanoparticles with spinel structure to possess an overpotential as low as 328 mV at a current density of 10 mA cm^{-2} in 1 M KOH.[17] In principal, Co_3O_4 suffers, like TMOs in general, from poor intrinsic electronic conductivity.[18] However, this drawback can be overcome by doping[19] and/or nanostructuring strategies.[20] It is described in literature that the (nano-) morphology of Co_3O_4 plays a significant role for the overall electrocatalytic performance since it affects the effective surface area and migration paths of the charge carriers.[21] In a comparative study between mesoporous and compact/dense high entropy oxide (HEO) thin films applied as OER catalysts, it has been demonstrated that indeed nanostructured materials possess substantially lower charge transfer resistances and an increased number of catalytically active reaction sites resulting in reduced overpotentials.[22] In 2018, Liu's group has synthesized Co_3O_4 structures in form of nanosheets, nanoparticles, and nanospheres and performed electrochemical measurements in 1 M KOH.[23] The obtained overpotentials varied from 300 mV to 400 mV, which indicated that the nanomorphology significantly impacted the electrochemical performance mainly *via* changes in the contact area between the surface of the electrocatalyst and the electrolyte. In another study, the effect of crystal faceting of Co_3O_4 was investigated by exposing different crystal planes to the electrolyte and it was found that the ratio of Co^{3+} and Co^{2+} ions differs with varied crystal planes, which in turn significantly affected the activity of the OER.[24] Furthermore, a recent work of Haase *et al.*, who quantitatively investigated a size-dependent catalytic activity of $CoO_x(OH)_y$ nanoparticles, uncovered a size-dependent oxidation activity leading to a near-surface Co–O bond contraction during OER.[21] It has also been revealed that this sort of contraction as well as the accumulation of oxidatively induced charge carriers increases with the decrease in nanoparticle size. Consequently,

nano- and mesostructuring can be considered as promising strategies to improve the electrocatalytic activity of cobalt oxides. Mesoporous networks provide additional catalytically active reaction centres due to increase of the internal surface area, which represents the contact area with the electrolyte. Additionally, mesoporous frameworks shorten the transfer paths of migrating charge carriers and endows the material with mechanical flexibility: all parameters allowing for the tailor and control of the material properties.[25] Making use of the evaporation-induced self-assembly (EISA) process of metallic precursors and block-copolymers, dip-coating is an easy-to-handle and low-cost technique to create high-quality mesoporous thin films by soft-templating.[26] Amphiphilic surfactants, such as the di-block copolymer Kraton LiquidTM-poly(ethylene-*co*-butylene)-*block*-poly (ethylene oxide) (KLE-)[27] or the tri-block copolymer poly (ethylene oxide)$_{106}$-poly (propylene oxide)$_{70}$-poly (ethylene oxide)$_{106}$ (PEO_{106}-PPO_{70}-PEO_{106}, Pluronic$^{®}$ F-127) contribute to microphase separation by generation of micellular structures owing to their hydrophilic and hydrophobic character.[26] Upon dip-coating, the solution, which contains the dissolved block-copolymer and metal precursors, can be readily coated on polar and non-polar substrates, and with the formation and self-assembly of micelles along with the hydrolysis and condensation reactions of the inorganic precursors, an amorphous and mesostructured hybrid network can be formed (Fig. 1). By subsequent thermal treatment of the as-deposited amorphous composite, the decomposition of the organic template and crystallisation of the inorganic nanoarchitecture are initiated (Fig. 1).[28] In terms of preparation of mesoporous Co_3O_4 (further ascribed to meso-Co_3O_4) by soft-templating, structure directing agents (SDA) from the Pluronic$^{®}$ family have been utilized in a few studies. In Song's work, poly(ethylene glycol)-*block*-poly(propylene glycol)-*block*-poly(ethylene glycol) (PEO_{20}–PPO_{70}–PEO_{20}, Pluronic$^{®}$ P-123) was used as surfactant to prepare Ni- and Mn-doped meso-Co_3O_4 with pore sizes ranging from 7.7 nm to 12.3 nm.[29] It was also reported by Feng *et al.* that mesoporous Co_3O_4/Fe_3O_4 nanocomposite materials (pore diameter from 3.4 nm to
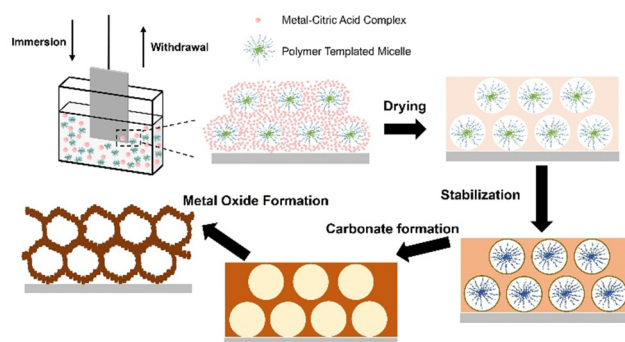

Fig. 1 Schematic drawing of the consecutive steps during the applied dip-coating process: the drying process leads to an amorphous hybrid structure, followed by formation of a composite network, which is stabilized through condensation at 200 °C and further transformed into a nanocrystalline mesoporous framework after annealing at 300 °C (template removal and calcination).

6.1 nm) can be synthesized through a ligand-assisted self-assembly method using Pluronic® P-123 in which the synthesized compound exhibited a relatively low overpotential of 322 mV at 10 mA cm^{-2} in 1 M KOH.[30] Utilization of Pluronic® F-127 as SDA has also been reported to produce mesoporous metal oxides,[31] however never in the context of direct fabrication of crack-free and structurally intact meso-Co_3O_4 thin film electrodes for application in OER catalysis. Eckhardt *et al.* developed a general synthesis concept to prepare various mesoporous metal oxides using citric acid as chelating agent.[32] The presented method addresses the general drawback that inorganic precursors with good solubility in polar solvent often decompose (in the case of cobalt nitrate hexahydrate, $T_m = 55$ °C) during calcination before they can be stabilized *e.g.* by complexation. This typically leads to failure of production of both the desired metal oxide phase and nanomorphology. They reported that the precursor-citric acid complex was transformed into a metal carbonate phase by applying relatively low temperatures (in the case of cobalt carbonate, the range is between 170 °C and 250 °C) in air. Since carbonates are thermally more stable, they can be directly converted into the corresponding metal oxide structure at elevated temperatures.[32,33] Such transition from carbonates to oxides has been proven to be beneficial to the formation of porous structures.[34] This modified EISA method has mostly been adaptable for costume polymer materials (such as PIB-PEO or KLE) as they typically possess a tailored hydrophilic–hydrophobic character and higher thermal stability[35] compared to commercial polymers, such as from the Pluronic family. Hence, the main challenges which have to be considered by the selection of the SDA in terms of forming mesoporous structures are the hydrophilicity of the formed complex and the volume change upon the conversion from the precursor to the oxide.[36] As consequence, it was reported that utilization of common commercial templates (like Pluronic® F-127) did not result in mesoporous networks based on the prior formation of a metal nitrate–citric acid complex.[32–34]

However, in this study, the compatibility of both Pluronic® F-127 and citric acid for the direct preparation of meso-Co_3O_4 thin films on conductive substrates by dip-coating is reported. The successful preparation of mesoporous Co_3O_4 networks with Pluronic® F-127 is highly indicated since the polymer is comparatively cheap and its usage results in the formation of small mesopores leading to high surface areas.

The underlying study aims to demonstrate a novel synthesis approach for the creation of meso-Co_3O_4 thin film electrodes readily available on conductive substrates by utilizing both Pluronic® F-127 and citric acid upon the EISA process. By correlating the electrochemical performance to the nanomorphology, crystallographic structure, elemental bulk and surface composition, and atomic configuration in/on meso-Co_3O_4, it was found that high surface areas, short charge carrier migration paths, phase-purity, and the presence of defective oxides and Co^{3+} species are synergistically responsible for the enhanced OER activity.

Experimental

Chemicals

All chemicals were of analytical grade and used as received: cobalt(II) nitrate hexahydrate ($Co(NO_3)_2 \cdot 6H_2O$, 99.999%, Sigma Aldrich), citric acid ($\geq$99.5%, Carl Roth), Pluronic® F-127 ($M_w = 12\,600$ g mol^{-1}, Sigma Aldrich), ethanol (EtOH, $\geq$99.8%, Sigma Aldrich), potassium hydroxide (KOH, 1 mol L^{-1}, Carl Roth).

Sample preparation

For preparation of the dip-coating solution, which was adapted from Eckhardt *et al.*,[33] 276 mg $Co(NO_3)_2 \cdot 6H_2O$, 91.3 mg citric acid (CA), and 45 mg Pluronic® F-127 were dissolved in a mixture of 1.2 mL EtOH and 1.1 mL of double distilled H_2O. The solution was stirred using a magnetic stirrer for 30 min until a transparent and homogeneous solution was obtained. Before dip-coating, all substrates were initially cleaned with ethanol and acetone, and subsequently treated by an UV ozone cleaner (L2002A3-EU, Ossila) to remove organic surface contamination. Dip-coating was conducted with a dip-coater (L2006A1-EU, Ossila) equipped with a self-constructed chamber for control of the relative humidity at 15% RH for a homogenous thin film deposition. Fluorine-doped tin oxide (FTO) glass (from XOP glass) and silicon (100) wafers (from Silchem, n-type, resistivity <3 mΩ) were used as substrates applying a constant withdrawal speed between 2–8 mm s^{-1} upon dip-coating.

After dip-coating, the samples were dried in the humidity-controlled chamber for 5 min, then transferred into a pre-heated muffle furnace (Nabertherm LT3/11) set to 125 °C, und subsequently heated to 200 °C with the rate of 10 °C min^{-1} and hold for 1 h, which was necessary for the formation of metal carbonates. A following heating step to 300 °C within 10 min was proceeded, and this temperature was kept for additional 30 min. The synthetic procedure of meso-Co_3O_4 is schematically illustrated in Fig. 1.

Structural characterization

Scanning electron microscopy (SEM) investigations were carried out on a Philips XL30 FEG at acceleration voltages of 30 keV and working distances of 3–4 cm. In transmission electron microscopy (TEM) measurements, post-treatment of samples was conducted by using a razor blade. Flakes of the thin film were scraped off the silicon substrate and collected in a small sample glass. After adding 2 mL of ethanol, they were dispersed with the help of an ultrasonic bath. The dispersion was allowed to settle for 20 s to separate large particles. Two to three droplets of the upper part of the dispersion were applied on a carbon coated copper grid (holey type, Plano GmbH, Wetzlar, Germany). After evaporation of the ethanol, the samples were coated with a thin carbon film (carbon coater MED 010, Bal-Tec AG, Balzers, Liechtenstein) to eliminate charging from the incident electron beam in the TEM. Examination of the samples were performed using the TEM mode in a FEG TEM (JEM2100F, JEOL Ltd, Tokyo, Japan). X-ray diffraction was conducted on a Rigaku Smartlab (Cu Kα radiation)

diffractometer in a grazing incidence setup with θ source = 5°. Data were recorded between 10° and 60° (in units of 2θ) using a step size of 0.01°. We acquired topography images of the sample surface using an atomic force microscope (AFM) from Bruker (Santa Barbara, CA, Type: Icon Dimension) in the amplitude modulation mode in combination with a PPP-FMAuD cantilever (NanoAndMore GmbH, Wetzlar, Germany). In this mode, the sample surface is tracked by keeping the oscillation amplitude of the cantilever at a constant value (here: 63% of the free amplitude A_0, A_0 = 206 nm) varying the tip-sample distance. The cantilever had a nominal spring constant of 1.6 N m^{-1} as determined by the thermal noise method,[37] a resonance frequency of 71.966 kHz with a guaranteed tip radius of <10 nm provided by the manufacturer. The scan speed of the tip was set to 2 μm s^{-1}. The inverse optical lever sensitivity of the cantilever was calibrated using a sapphire sample. By pushing the tip towards the stiff surface, the oscillation amplitude detected by the photodiode (in the unit of volts) could be correlated with the motion (in the unit of nanometres) of the z-piezo and resulted in S = 137 nm V^{-1}. Topography images were first-order flattened to remove sample tilt and to correct for thermal drift which is unavoidable during image acquisition in ambient conditions. The film thicknesses were determined with a Bruker profilometer (Dektak XT) using a scan rate of 10 μm s^{-1} and a stylus force of 3 mg. For each sample, the thickness was collected on three different positions on the sample surface, and the values were averaged assuming an error of ±10 nm for determination of the film thickness.

Spectroscopic characterization

X-Ray photoelectron spectroscopy (XPS) experiments were accomplished in a vacuum-cluster tool on a ULVAC-PHI VersaProbe II instrument with a base pressure in the analysis chamber below 5×10^{-9} mbar. Monochromatized Al Kα radiation (1486.6 eV) was utilized as excitation source. Detailed spectra were measured applying a pass energy of 23.5 eV and a step size of 0.1 eV per step. Survey spectra were determined by applying a pass energy of 187.9 eV and the step size was set to by 0.8 eV. Binding energy calibration was performed by setting the Au 4f$_{7/2}$ emission of Au foil to 84.0 eV. Backgrounds of the acquired spectra were subtracted by using the Shirley method in CasaXPS,[38] version 2.3.25. Raman spectra were acquired with a LabRAM Horiba HR-800 Raman microscope with a 785 nm laser. Using a neutral density filter the power density was 25 mW at a spot size of $\approx$ 1.5 μm for a 50× LWD objective. As a 600 g mm^{-1} grating was chosen, the diameter of the pinhole was set to 200 μm and the entrance slit size to 100 μm. Spectra were accumulated 15 times for 10 s acquisition time per scan. For each sample equivalent spectra were collected on two different positions.

Optical characterization

UV-visible light spectroscopy was accomplished by a UV/Vis/NIR spectrometer from Agilent (Cary 7000). The absorption spectra were determined by measuring the transmittance between 300 nm and 2500 nm using a scan speed of 600 nm min^{-1} and 6° angle of incidence. By conversion of the corresponding absorbance spectra into the Tauc plots, the direct and indirect optical band gaps were derived by extrapolation of the slope with the intercept of the x-axis and the baseline of the plot, respectively.

Electrochemical measurements

All electrochemical experiments were conducted in a three-electrode setup (Zahner cell PECC-2) utilizing a Hg/HgO reference electrode and a platinum wire ring as counter electrode. The electrolyte was chosen to be 1 M KOH (pH $\approx$ 13.6). The potential was controlled by a GAMRY Interface 1000E potentiostat. Linear sweep voltammetry (LSV) was acquired between 0.9 V and 1.9 V versus RHE using a step size of 1 mV and a scan rate of 10 mV s^{-1}. Cyclic voltammetry (CV) was conducted between 0.6 V and 1.5 V versus RHE with a scan rate of 100 mV s^{-1} and a step size of 1 mV. The potentials in the LSV curves were corrected by iR-drop through evaluation of the electrolyte resistance derived from electrochemical impedance spectroscopy (EIS) data. EIS was measured at 1.64 V versus RHE for applied frequencies between 100 kHz and 1 Hz and by using an AC modulation of 10 mV. The double-layer capacitance was derived after the method of McCrory[39] by analysing the differential current densities at distinct scan rates of 20–200 mV s^{-1} in a non-faradaic potential range (found between 0.57 V and 0.67 V vs. RHE). Chronopotentiometry (CP) was carried out at constant current density of 10 mA cm^{-2} for 14 000 s. The reference potential of the Hg/HgO electrode was measured against a reversible hydrogen electrode (RHE, HydroFlex, Gaskatel) in the above-mentioned electrolyte before the experiments and used as conversion value taking the Nernst equation into account.

Results and discussion

Structural properties

The surface structure and morphology were reported to have major impact on the electronic conductivity and OER activity, which was demonstrated, for example for mesoporous HEO thin films also prepared by dip-coating and soft-templating.[22] In order to investigate these relevant surface structures and to reveal the impact of utilizing citric acid as complexing agent, scanning electron microscopy (SEM) were performed for Co_3O_4 samples treated at distinct calcination temperatures as well as in the presence (Fig. 2(A)) and absence of citric acid (Fig. 2(B)). As shown in Fig. 2(A), the surface morphology of the meso-Co_3O_4 thin films calcined at 300 °C for 30 min displays a homogenous and crack-free mesostructured framework with nanopores of 16 nm in average size (see ESI,† Fig. S1 B1–B2 for mesopore size determination). The pore size distribution in the underlying thin films was found to be slightly different compared to Pluronic® F-127 templated samples from literature, which is attributed to the balance of interaction between the phase separation effects,[40,41] the stabilization effect of citric acid, and application of distinct annealing protocols.
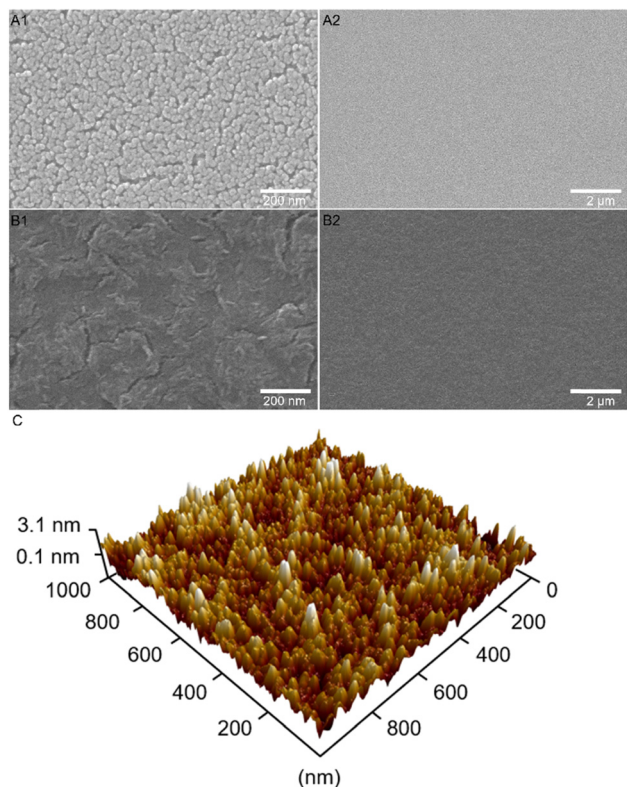
Fig. 2 SEM images of Co_3O_4 thin films recorded at distinct magnifications prepared (A1) and (A2) with citric acid (mesoporous thin films) and (B1) and (B2) without citric acid (dense thin films). Both materials were pre-heated for 10 min at 125 °C, stabilized at 200 °C for 1 h, and calcined at 300 °C for 30 min. (C) Three-dimensional representation of the topography of meso-Co_3O_4 thin films (using citric acid) measured by atomic force microscopy in the amplitude modulation mode.

For investigating the morphological evolution of the surface upon annealing, meso-Co_3O_4 samples were treated at 400 °C, 500 °C, and 600 °C and the corresponding top-view SEM pictures are presented in the ESI† (Fig. S2). Fig. S2 (ESI†) illustrates that the size of the pore wall domains and the average pore diameter increases with annealing temperature, which was assigned to the thermally induced growth of nanocrystals.[42–44] After delicate optimisation of the intrinsic (e.g., solution and precursor concentration) and extrinsic (e.g., humidity, temperature, and withdrawal speed) parameters, homogeneous and reproducible surface morphologies were formed at each temperature, showing neither macro- nor mesoscopic cracks. In this study, meso-Co_3O_4 annealed at 300 °C for 30 min was chosen as control sample, since the dependency of the OER activity of nanostructured TMOs on their crystallinity and surface area (which is a function of calcination temperature for soft-templated metal oxides) have already been thoroughly investigated in literature.[39–42] The temperature dependent OER activity of mesoporous oxides was, for example, studied for XCo_2O_4 (X = Mn, Ni, and Zn)[45] and IrO_2[46,47] revealing ideal calcination temperatures between 300 °C and 375 °C depending on the used surfactants. It is known that the OER activity benefits from high surface areas

and nanocrystalline and/or partially amorphous structures due to the presence of unsaturated reaction sites, such as catalytically active oxygen vacancies.[48,49]

Fig. 2(B_1)–(B_3) demonstrates the top-view SEM images of Co_3O_4 annealed at 300 °C without usage of citric acid. It can be observed that no mesoporous framework has been formed in the absence of citric acid giving empirical evidence that this stabiliser is essential for the complexation of cobalt ions during the stabilisation and annealing process. Citric acid is vital for the formation of a mesoporous framework.

Interestingly, most mesoporous TMO thin films are reported to be prepared without chelating agents such as citric acid, as was shown, for example, for the synthesis of ordered mesoporous $CoFe_2O_4$,[50] $CuFe_2O_4$,[51] indium tin oxide,[52] and high-entropy oxide.[53] In conclusion, the feasibility of forming those mesoporous TMOs thin films strongly depends on the complexation behaviour of the corresponding TM. The formation of TMO mesostructures does not only depends on experimental conditions, but also on the metal-oxide sources, solvent composition, and coordinating agents.[36]

Atomic force microscopy (AFM) in the amplitude modulation mode was accomplished to visualize and analysis the three-dimensional surface topography of the meso-Co_3O_4 sample (Fig. 2(C)). It is exhibited that the sample possesses a highly nanoporous surface structure with peak elevations representing the pore walls. The sample exhibited a typical root-mean-square roughness of 0.82 nm measured within an area of 1000×1000 nm^2 indicating a rather smooth and uniform surface morphology in spite of the fact that mesopores are present, thus further proving the homogeneity of the produced thin films. Additional topography and phase-mode images of the sample can be found in the ESI† (Fig. S3). The thickness of the meso-Co_3O_4 thin film was measured to be 240 ± 10 nm on silicon substrate by profilometry (Fig. S4, ESI†).

To further study the structural bulk features of meso-Co_3O_4 on the nanoscale, TEM was carried out as shown in Fig. 3 and Fig. S5 (ESI†). As indicated, the material consists of 3–4 nm sized crystals embedded in an amorphous matrix (Fig. 3(B)). The HR-TEM image (compare inverse fast Fourier transition IFFT images in Fig. 3(B)) displays the lattice fringes associated to (311) and (400) crystal planes. Also, the selected area electron diffraction (SAED) pattern can be indexed applying the lattice constant of the cubic Co_3O_4 spinel phase, which was determined to be a = 8.05 Å being in good accordance with literature.[54] To further assess the crystallographic structure, gracing-incidence wide-angle X-ray diffraction (GIWAXS) analysis was conducted (Fig. 4(A)). Six characteristic diffraction peaks at 19.2°, 31.0°, 36.7°, 44.9°, 60.4°, and 65.4° were identified to correspond to the (111)-, (220)-, (311)-, (400)-, (511)-, and (440)- lattice plane, respectively, which were consistently assigned to the cubic Co_3O_4 spinel phase (JCPDS no. 42-1467). No diffraction peaks of the as-prepared samples were related to Co, CoO, CoOOH, and/or $Co(OH)_2$ phases. The general low signal-to-noise ratio in the diffraction patterns has to be attributed to the low crystallinity of the thin films, which agrees with TEM observations (Fig. 3) and the fact that
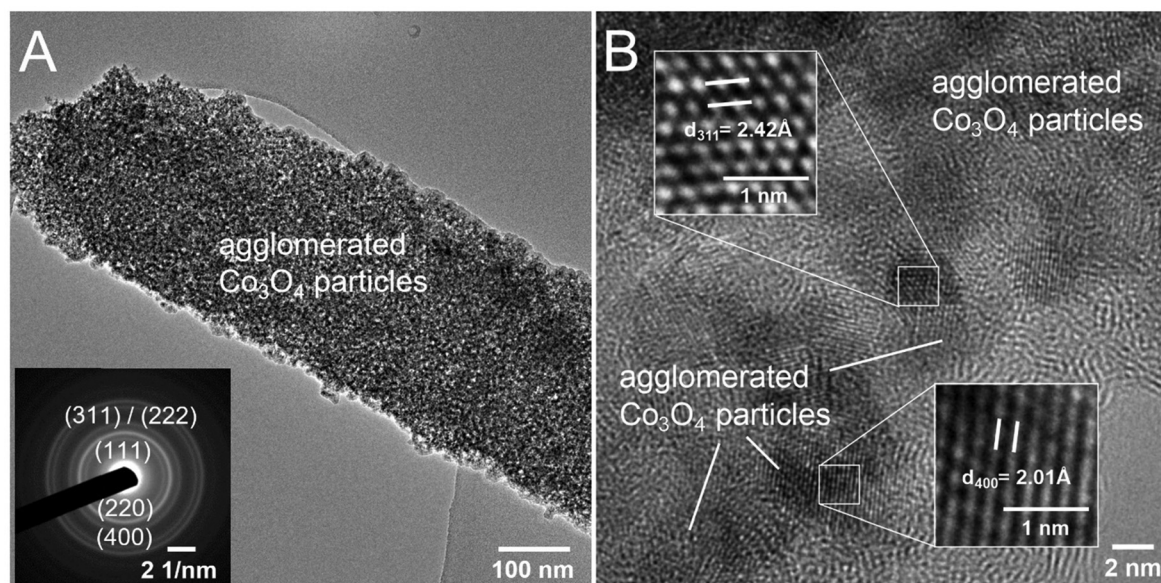
Fig. 3 (A) TEM and (B) HRTEM images of meso-Co_3O_4 thin films. Inset in (A) shows SAED patterns from the bulk area indexed in agreement with the cubic spinel phase. (B) IFFT images from the marked areas including the indicated atomic distances for (311) and (400) lattice planes.
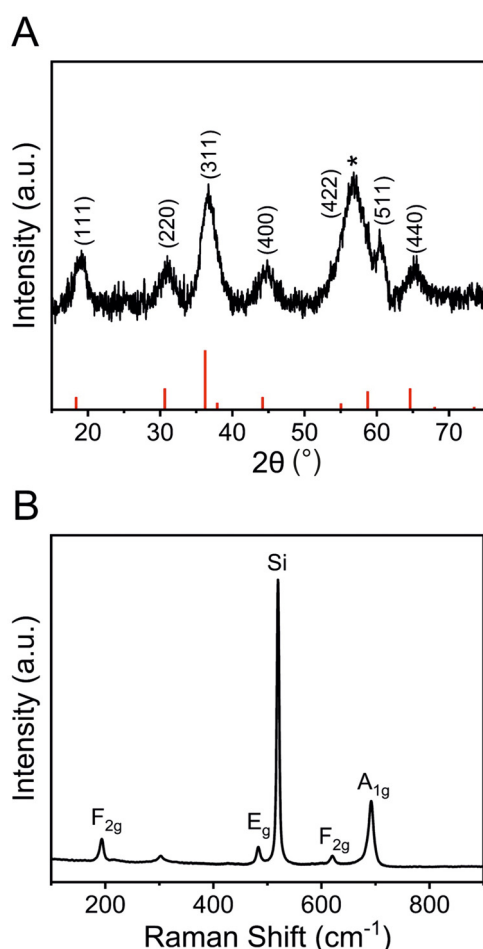

Fig. 4 (A) GIWAXS pattern including reference bars (red lines) from JCPDS no. 42-1467 and the asterisk indicating the diffraction peak by the silicon substrate, and (B) Raman spectrum of the cubic spinel meso-Co_3O_4 thin film calcined at 300 °C for 30 min.

the films were treated at low calcination temperatures of 300 °C for a relative short time frame of 30 min. The average crystallite size of the Co_3O_4 sample was determined by applying the Scherer equation to the (311) peak and was evaluated to be 3.7 nm allowing the description as a quantum-sized nanocrystalline system (nanoconfinement effect). Raman spectroscopy, which is more sensitive to the formation of secondary phases, was carried out to further elucidate and verify the phase-purity, and thus, to exclude the presence of additional crystal phases. Co_3O_4 typically crystallizes in the spinel structure $Co^{2+}(Co^{3+})_2O_4^{2-}$ with Co^{2+} located at tetrahedral sites (A-site) and Co^{3+} at octahedral sites (B-site), respectively, considering a normal spinel configuration.[55] According to Rousseau et al., the vibrational modes at $k = 0$ can be reduced from a 42-dimensional representation of Γ into:[56]

$$\Gamma = A_{1g} + E_g + 3F_{2g} + 5F_{1u} + 2A_{2u} + 2E_u + 2F_{2u}$$

for which only the A_{1g}, E_g, and F_{2g} phonon modes are Raman active.[57] The Raman spectrum of the at 300 °C calcined meso-Co_3O_4 thin films is shown in Fig. 4(B). Four Raman peaks appearing at 483 cm^{-1}, 193 cm^{-1}, 620 cm^{-1}, and 693 cm^{-1} correspond to the E_g, F_{2g}, and A_{1g} bands of the cubic Co_3O_4 spinel phase. The highest peak at 520 cm^{-1} is attributed to the signal arising from the silicon substrate (Fig. S6, ESI†). According to the Raman spectrum, the meso-Co_3O_4 samples can be considered as phase-pure and the data additionally support the XRD and TEM results.

Surface analysis

The chemical oxidation states and binding configurations of the elements on the surface of meso-Co_3O_4 were analysed through X-ray photoelectron spectroscopy (XPS). The pronounced peaks in the survey spectrum (Fig. S7A, ESI†) correspond to the photoemission of cobalt and oxygen orbitals,[58]
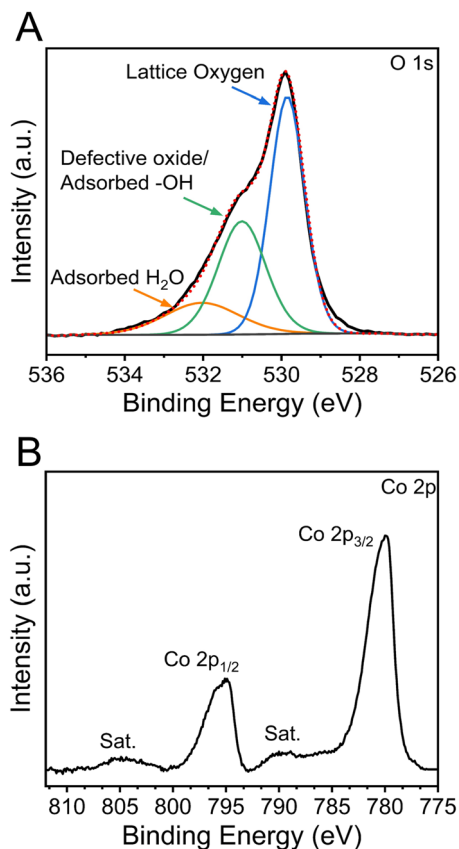
Fig. 5 XPS spectra of the (A) O 1s spectrum (black) with the fitting curves (red dots) including fitting component of lattice oxygen (blue), oxygen defects or adsorbed hydroxyl groups (green), adsorbed water (orange). (B) Co 2p photoemission lines of meso-Co_3O_4 showing spin−orbital splitting and the presence of satellites.

which can be found along with the carbon C 1s signal (Fig. S7B, ESI†) at 285 eV. For the detailed scan of the O 1s spectrum (Fig. 5(A)) recorded between 538 eV and 524 eV in terms of binding energy, the main peak at 529.8 eV can be attributed to lattice oxide (*i.e.*, metal oxide), and the less intense peak at 531.0 eV presents hydroxide hydrated and/or potential defective oxide groups.[59] It has been reported that the electrocatalytic activities of spinel metal oxides largely benefit from the presence of defective oxygen sites, *e.g.*, in the form of oxygen vacancies, which are more likely to be present in nanocrystalline cobalt oxide samples due to the less organized nature on the molecular scale.[60,61] It has also been reported that the peak located at 532.3 eV can be ascribed to the signals of organic ligands, such C–O, which most likely originate from the residual carbonized Pluronic® F-127.[59] In the Co 2p spectra (Fig. 5(B)), two prominent peaks located at the binding energy of ∼795 eV and ∼780 eV are observed, which were attributed to the Co $2p_{1/2}$ and Co $2p_{3/2}$ spin-orbital splitting.[62] The associated charge-transfer satellites at 805 eV and 790 eV indicate that cobalt ions are present in the oxidation state Co^{3+} and Co^{2+} occupying both tetrahedral and octahedral sites in the spinel configuration.

UV-vis spectroscopy was additionally conducted to analyse the optical band gap energy of the material and to determine the energy diagram. Therefore, the absorbance spectrum (Fig. S8A, ESI†) was converted into a Tauc plot (Fig. S8B, ESI†). By extrapolation of the recorded data to the *x*-axis, the optical band gap energy of meso-Co_3O_4 was determined to be 1.5 eV and 2.1 eV, when assuming direct optical transitions. It is well known that in the case of spinel Co_3O_4, the valence band has a strong oxygen 2p character, and the conduction band consists of Co(II) 3d orbitals, while a sub-band inside the band gap is formed due to the presence of Co(III) centres. As the Co(III) d states are closer to the p states of O $(^{2-})$, the system can undergo an electron transition from $p(O^{2-})$ to $e_g(Co^{3+})$.[63] For the pure Co_3O_4 sample, the direct allowed optical transitions can be divided into two excitations from $p(O^{2-})$ to $e_g(Co^{3+})$ and $p(O^{2-})$ to $e_g(Co^{2+})$ levels, corresponding to optical band gap energies found at 1.5 eV and 2.1 eV (Fig. S8B, ESI†), respectively.[64,65] However, according to the study of Qiao *et al.*,[66] in the lower range of photon energies (between 0.5 eV and 1.0 eV), the fundamental band gap of Co_3O_4 was demonstrated to be located at 0.74 eV, as verified by using synergetic infrared optical and *in situ* photoemission spectroscopy combined with density functional theory (DFT) calculations. The authors ascribed the energy band gap of Co_3O_4 to a direct dipole-forbidden d–d transition between tetrahedral-site Co^{2+} cations.[66] Such a related significant absorbance characteristic in a wavelength range between 1000 nm and 2500 nm has also been observed for the underlying meso-Co_3O_4 thin films (Fig. S8A, ESI†). The main absorbance feature starts at an energy of 0.9 eV (Fig. S8B, ESI†). These data are in accordance with the study by Lohaus *et al.*, also reporting characteristic absorption maxima at 0.8 eV and 1.7 eV.[58] Hence, the evaluated band gap energy of 0.9 eV was used to draw the energy diagram as shown in Fig. 6. Due to the nanoconfinement effect, a band gap widening is likely to being present for the mesostructured
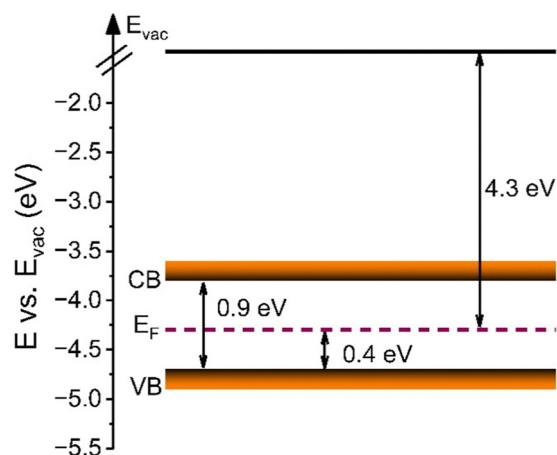

Fig. 6 Band energy diagram representing the VB, CB, and EF alignment derived from determination of the valence band maximum by XPS analysis and UV-vis spectroscopy. The energy gap between CB and VB illustrates the direct optical band gap energy derived by UV-vis spectroscopy for the meso-Co_3O_4 thin film.

Co_3O_4 since the crystallite size was analysed to be 3–4 nm (by GIWAXS and TEM). For example, this phenomenon was also observed for quantum-sized TiO_2 particles.[67,68] Based on the evaluated direct optical band gap energies and the valence band maximum (VBM) along with the analysed work function (see Fig. S9, ESI†) derived from XPS experiments, the energy diagram of the meso-Co_3O_4 was constructed (Fig. 6). It can be stated according to the energy diagram that meso-Co_3O_4 is a p-type semiconductor as its Fermi level, which was determined by measuring the work function, is close to the VBM (0.4 eV distance), which agrees well with literature data.[58]

Electrochemistry

To show the beneficial effect of mesostructuring on the electrochemical properties and the OER activity of sol–gel-derived Co_3O_4 thin films, mesoporous (with citric acid) and dense Co_3O_4 thin films (without citric acid, see Fig. 2) were analysed and compared by linear sweep voltammetry (LSV) in 1 M KOH in a potential range between 1.0 V and 1.7 V vs. RHE (Fig. 7(A)). For comparison, a nickel oxide (NiO) thin film known to form highly reactive NiOOH species under OER conditions in alkaline media,[14] was characterized as reference material under very same conditions as illustrated in Fig. 7(A). An anodic peak present at 1.45 V reveals the oxidation of electrocatalytically active surface species, which was attributed to the oxidation of Co(III) to Co(IV) ions, where the Co(IV) in the form of CoO_2 is suggested as the active catalytic species.[69] Such behaviour has also been reported by Surendranath et al. who describes that the generation of Co(IV) species is a further oxidation channel besides the oxidation of Co(II) to Co(III).[70] From the LSV curves, the onset potential of the current density was determined to be 1.50 V vs. RHE, which is a relatively low value compared with the data from literature usually reporting onsets between 1.52 and 1.56 V vs. RHE.[71] The reason for that is most likely ascribed to the mesostructure of the Co_3O_4 sample facilitating the involved charge transfer at the interface, which will be discussed in more detail in the electrochemical impedance spectroscopy (EIS) section. The overpotential of the OER is usually determined at a geometric current density of 10 mA cm^{-2}, thus making a general comparison of distinct OER electrocatalysts possible. The presented meso-Co_3O_4 thin film exhibits a voltage of 1.56 V vs. RHE identified at current density of 10 mA cm^{-2} and corresponding to an overpotential of 340 mV. This is a comparatively low value among cobalt-oxide-based catalysts from previous studies reporting overpotentials ranging from 310 mV to 400 mV (at the same current density), and even exceed the OER performance of cobalt containing, mesoporous HEO thin films.[22,72] The dense Co_3O_4 thin films, produced in the absence of citric acid as chelating agent, exhibit an overpotential of 355 mV, which is higher compared to the mesoporous thin film, and exceed the performance of NiO (η_{10} = 450 mV). The high OER activity can be assigned to the large surface area arising from the ex- and internal mesoporous structure offering a plenty of reaction sites, most likely in the form of defective oxides and Co^{3+} ions (the presence which was proofed by XPS) preferably occupying

octahedral sites in the spinel structure.[73] Co^{3+} is known to be the active species in cobalt oxide-based spinel structures due to the increased charging, appropriate adsorption energetics of the reaction intermediates, and the preferred localisation of octahedrally coordinated units at surface sites of an electrocatalyst.[74] As described earlier, the intrinsic properties (e.g., electronic conductivity) have a tremendous impact on the charge carrier transfer processes, and thus the overall OER performance. In order to interpret the kinetics for the oxygen evolution reaction and to compare the meso-Co_3O_4 with the performance of other electrocatalysts, the Tafel slope (Fig. 7(B)) was determined. Here, the slope was determined to be 57 mV dec^{-1}, which is a rather low value compared to other cobalt oxide-based materials typically ranging between 60 mV dec^{-1} and 70 mV dec^{-1}.[72] The dense Co_3O_4 thin film electrocatalyst showed a value of (62 mV dec^{-1}). The low Tafel slope values suggest that the rate-determining step for OER is an activation-controlled process involving a reversible one-electron transfer as reported in literature.[75] Prospective work will focus on operando analysis of the meso-Co_3O_4 to analyse the catalytically active surface phase in detail.

Cyclic voltammetry (CV) was measured in 1 M KOH at a scan rate of 100 mV s^{-1} for 50 cycles. As indicated in Fig. 7(C), pronounced redox peaks were observed in the potential range between 0.6 V and 1.5 V vs. RHE. Note that the broad peak appearing in the range of 0.8 V to 1.1 V, represents the redox couple of Co(II) (most likely located at the tetrahedral sites) and Co(III). It is widely agreed that the surface of Co_3O_4 experiences a partial oxidation into a CoOOH phase,[72,76] which is in accordance with the Tafel plot evaluation also suggesting a possible formation of oxyhydroxide species. As mentioned in the discussion for LSV, Co(III) species – preferentially located at octahedral sites – are catalytically active towards OH-oxidation during OER.[70] The main oxidation peaks of mesoporous and dense Co_3O_4 were observed with a difference in the peak potential of 80 mV (Fig. 7(C)), which can be most likely ascribed to the change in surface morphology, resulting increased surface areas (see Fig. 2 and 7(D)), and thus, enhanced surface reactivity. Upon cyclisation, the oxidation peaks decrease substantially from the 1st to the 50th cycle (Fig. 7(C)) indicating the consumption and thus reduced amount of Co(II) active sites on the (internal) surface.[72]

The electrochemical active surface area (ECSA) is another important electrochemical parameter for the characterisation of electrocatalysts, as it provides information about the mesoporous architecture and amount of reaction sites at the surface.[77] The ECSA is directly related to the ratio of the double-layer capacitance (C_{DL}) and specific capacitance (C_s):

$$ECSA = \frac{C_{DL}}{C_s}$$

By measuring scan rate-dependent cyclic voltammetry curves (Fig. S10, ESI†), the difference in the anodic current density collected at varied scan rates were plotted in Fig. 7(D). From the slopes of the linear fittings, C_{DL} can be directly
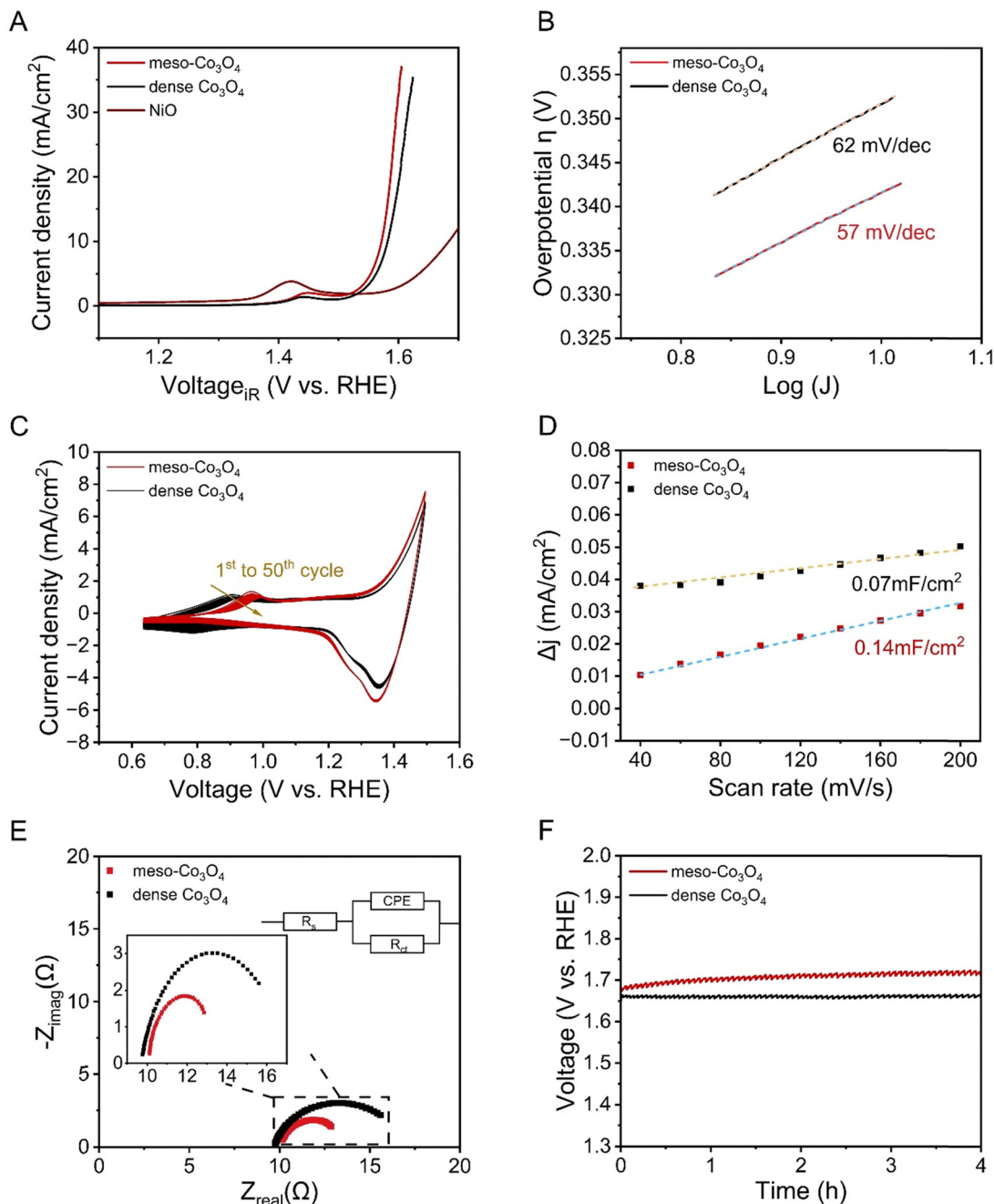
Fig. 7 Electrochemical characterization of mesoporous and dense Co_3O_4 thin films including (A) linear sweep voltammetry curves collected at a scan rate of 10 mV s^{-1} and the performance of the NiO films taken from reference[14] as comparison, (B) Tafel plot analysis, (C) 50 cyclic voltammetry scans measured from 0.6 to 1.5 V and recorded at 100 mV s^{-1}, (D) differential current densities plotted *versus* the scan rate for the evaluation of the double layer capacitance, (E) the Nyquist plot determined by EIS at 1.6 V, and (F) chronopotentiometry analysis.

derived and were evaluated to be 0.14 mF and 0.07 mF, which correspond to an ESCA of 3.5 cm^2 and 1.75 cm^2 (when applying 40 μF cm^{-2} for C_S as suggested by McCrory *et al.*[39] for 1 M KOH electrolytes)[78] for mesoporous and dense Co_3O_4 samples, respectively. The comparison of the ECSA values suggests that the mesoporous structure provides an increased surface area, and thus, high amount of catalytically active reaction centres (compared to the dense thin films) contributing to the

improved OER performance. Additionally, the mesoporous network still might be partially blocked by non-degraded, residual carbon from the synthesis (see Fig. S7, ESI†).

EIS is a powerful tool to investigate the electrical resistance in an electrochemical device. Therefore, EIS was carried out for the mesoporous and dense Co_3O_4 samples at a fixed potential of 1.6 V *vs.* RHE and within a frequency range of 100 kHz to 1 Hz. Fig. 7(E) presents the Nyquist plots of the mesoporous

and dense Co_3O_4 thin film electrodes, and the upper inset shows the applied equivalent circuit including the solution resistance R_s (which was further used for the *iR*-correction of the current density applied in Fig. 7(A)), charge transfer resistance R_{ct}, and constant phase element (CPE). From EIS analysis the electrolyte resistance, R_s, was determined as 10 Ω, while the resistance of the charge transfer, R_{ct}, was calculated to be 3.5 Ω for mesoporous Co_3O_4. This value was found to be substantially lower compared to dense Co_3O_4 (7 Ω) and to most literature values,[71] indicating a significantly facilitated charge carrier transfer process from the catalyst to the electrolyte through the mesoporous architecture. Mesostructuring is known to ease the charge transport owing to the presence and accessibility of short charge carrier conduction paths, which are with respect to the surface, distances in the dimension of the pore walls. Graberg *et al.* reported for mesoporous ITO thin films that the electric conductivity increases for smaller mesopore sizes owing to a higher conduction path cross section.[52] Therefore, Pluronic® F-127 based mesoporous frameworks can be generally considered as a suitable nanoarchitecture for electrochemical applications, since this polymer is capable of creating mesopores below 15 nm (depending on the calcination temperature).[51] Conclusively, the presented citric acid route in combination with Pluronic® F-127 as SDA and cobalt nitrate as precursor, results in the formation of structurally intact Co_3O_4 mesostructures with good electronic conductivity, high surface areas, and thus a remarkable OER performance.

Since the stability of an electrocatalyst is an important property with respect to long-term applications,[79,80] chronopotentiometry at a constant applied current density of 10 mA cm^{-2} for 4 hours was performed in order to check the electrochemical stability of the material in alkaline solution. As shown in Fig. 7(F), a stable current response was obtained over four hours of CP analysis. Accordingly, the catalytic activity loss was determined to be only ∼2% with respect to the change in the measured electrode potential. For comparison, purely amorphous CoO_x is highly unstable upon proceeding OER owing to dissolution of metal ions into the electrolyte.[48] In the ESI† in Fig. S11, a SEM image of meso-Co_3O_4 after electrochemical performances is exhibited, which presents – despite of a few cracks on the macroscale – that the mesoporous morphology remains mainly structurally intact. However, the mesostructure seems to be less developed and densification has occurred most likely due to reconstruction of the surface upon electrochemical treatment, a phenomenon which was also observed for *e.g.* metal oxide nanofibers electrochemically treated in alkaline media.[44] For comparison, a tabular overview (Table S1, ESI†) of the OER performances of various nanostructured Co_3O_4 OER-electrocatalysts from literature are presented. The comparison under identical testing conditions (electrolyte, substrate, scan rate *etc.*) indicates that the underlying meso-Co_3O_4 thin films are among the best-performing wet-chemically derived electrocatalysts with promising stability for driving the OER reaction in water splitting under alkaline conditions.

Conclusions

In the search for high-performance electrocatalysts possessing high surface areas aiming for high reactivity, the dip-coating and soft-templating method offers an easy-to-handle and scalable technology to produce uniform and mesoporous Co_3O_4 networks on conductive substrates. Investigations towards the bulk and surface morphology, crystallography, elemental composition, and energetic alignment of the band positions were carried out for the mesoporous Co_3O_4 thin films in detail by combining several structural X-ray-based characterization techniques. The mesoporous Co_3O_4 framework was presented to possess a nanocrystalline bulk structure composed of quantum-sized nanocrystals (3–4 nm) hosting small, disordered mesopores averagely 16 nm in size. The mesostructuring resulted in a rich amount of accessible, electrochemically active reaction sites being the reason for the comparatively low overpotentials of 340 mV at a geometric current density of 10 mA cm^{-2} and when analysed in alkaline solution. Long-term stability tests by chronopotentiometry at 10 mA cm^{-2} presented stable oxygen evolution for at least four hours. In essence, the presented sol–gel process proves the compatibility of Pluronic® F-127 and citric acid in alcoholic solutions and the successful transformation of the amorphous composite into a nanocrystalline, mesoporous Co_3O_4 network during calcination. The presented synthesis approach can be understood as conceptual strategy to synthesize earth-abundant element-based high-surface-area TMOs thin film electrodes by utilization of a commercially available, inexpensive block-copolymer serving as organic template. This preparation route might be utilized to fabricate novel mesoporous metal oxide-based electrode systems, which benefit from the presence of large surfaces especially in the steadily developing research field of (electrochemical) energy conversion and storage.

Conflicts of interest

There are no conflicts to declare.

Acknowledgements

References

1 S. Chu and A. Majumdar, *Nature*, 2012, **488**, 294–303.
2 K. Khan, A. K. Tareen, M. Aslam, Y. Zhang, R. Wang, Z. Ouyang, Z. Gou and H. Zhang, *Nanoscale*, 2019, **11**, 21622–21678.
3 B. You and Y. Sun, *Acc. Chem. Res.*, 2018, **51**, 1571–1580.

4 J. Hou, Y. Wu, B. Zhang, S. Cao, Z. Li and L. Sun, *Adv. Funct. Mater.*, 2019, **29**, 1808367.

5 X. Peng, C. Pi, X. Zhang, S. Li, K. Huo and P. K. Chu, *Sustainable Energy Fuels*, 2019, **3**, 366–381.

6 K. Zhang and R. Zou, *Small*, 2021, **17**, 2100129.

7 S. Trasatti, *J. Electroanal. Chem. Interfacial Electrochem.*, 1980, **111**(1), 125–131.

8 Yu. E. Roginskaya, T. V. Varlamova, M. D. Goldstein, I. D. Belova, B. Sh Galyamov, R. R. Shifrina, V. A. Shepelin and V. N. Fateev, *Mater. Chem. Phys.*, 1991, **30**, 101–113.

9 Y. Lee, J. Suntivich, K. J. May, E. E. Perry and Y. Shao-Horn, *J. Phys. Chem. Lett.*, 2012, **3**, 399–404.

10 T. Audichon, T. W. Napporn, C. Canaff, C. Morais, C. Comminges and K. B. Kokoh, *J. Phys. Chem. C*, 2016, **120**, 2562–2573.

11 D. A. Corrigan, *J. Electrochem. Soc.*, 1987, **134**, 377.

12 M. Gong and H. Dai, *Nano Res.*, 2015, **8**, 23–39.

13 J. Zhao, J.-J. Zhang, Z.-Y. Li and X.-H. Bu, *Small*, 2020, **16**, 2003916.

14 J. Gallenberger, H. M. Fernández, A. Alkemper, M. Li, C. Tian, B. Kaiser and J. Philipp Hofmann, *Catal. Sci. Technol.*, 2023, **13**, 4693–4700.

15 H. Radinger, P. Connor, S. Tengeler, R. W. Stark, W. Jaegermann and B. Kaiser, *Chem. Mater.*, 2021, **33**, 8259–8266.

16 R. Elakkiya and G. Maduraiveeran, *Langmuir*, 2020, **36**, 4728–4736.

17 A. J. Esswein, M. J. McMurdo, P. N. Ross, A. T. Bell and T. D. Tilley, *J. Phys. Chem. C*, 2009, **113**, 15068–15072.

18 J. Yin, P. Zhou, L. An, L. Huang, C. Shao, J. Wang, H. Liu and P. Xi, *Nanoscale*, 2016, **8**, 1390–1400.

19 T. Tran-Phu, M. Chatti, J. Leverett, T. K. A. Nguyen, D. Simondson, D. A. Hoogeveen, A. Kiy, T. Duong, B. Johannessen, J. Meilak, P. Kluth, R. Amal, A. N. Simonov, R. K. Hocking, R. Daiyan and A. Tricoli, *Small*, 2023, **19**, 2208074.

20 A. Miquelot, M. Despotopoulou, C. Vahlas, C. Villeneuve, N. Dragoe, N. Prud'homme and O. Debieu, *Mater. Chem. Phys.*, 2020, **240**, 122059.

21 F. T. Haase, A. Bergmann, T. E. Jones, J. Timoshenko, A. Herzog, H. S. Jeon, C. Rettenmaier and B. R. Cuenya, *Nat. Energy*, 2022, **7**, 765–773.

22 M. Einert, M. Mellin, N. Bahadorani, C. Dietz, S. Lauterbach and J. P. Hofmann, *ACS Appl. Energy Mater.*, 2022, **5**, 717–730.

23 S. Liu, R. Zhang, W. Lv, F. Kong and W. Wang, *Int. J. Electrochem. Sci.*, 2018, 3843–3854.

24 Q. Liu, Z. Chen, Z. Yan, Y. Wang, E. Wang, S. Wang, S. Wang and G. Sun, *ChemElectroChem*, 2018, **5**, 1080–1086.

25 E. Celik, Y. Ma, T. Brezesinski and M. T. Elm, *Phys. Chem. Chem. Phys.*, 2021, **23**, 10706–10735.

26 B. Smarsly and M. Antonietti, *Eur. J. Inorg. Chem.*, 2006, 1111–1119.

27 A. Thomas, H. Schlaad, B. Smarsly and M. Antonietti, *Langmuir*, 2003, **19**, 4455–4459.

28 C. J. Brinker, Y. Lu, A. Sellinger and H. Fan, *Adv. Mater.*, 1999, **11**, 579–585.

29 W. Song, Z. Ren, S.-Y. Chen, Y. Meng, S. Biswas, P. Nandi, H. A. Elsen, P.-X. Gao and S. L. Suib, *ACS Appl. Mater. Interfaces*, 2016, **8**, 20802–20813.

30 D. Feng, T.-N. Gao, M. Fan, A. Li, K. Li, T. Wang, Q. Huo and Z.-A. Qiao, *NPG Asia Mater.*, 2018, **10**, 800–809.

31 M. S. Amer, M. A. Ghanem, P. Arunachalam, A. M. Al-Mayouf and T. A. Aljohani, *Adv. Mater. Lett.*, 2019, **10**, 136–144.

32 B. Eckhardt, E. Ortel, J. Polte, D. Bernsmeier, O. Görke, P. Strasser and R. Kraehnert, *Adv. Mater.*, 2012, **24**, 3115–3119.

33 B. Eckhardt, E. Ortel, D. Bernsmeier, J. Polte, P. Strasser, U. Vainio, F. Emmerling and R. Kraehnert, *Chem. Mater.*, 2013, **25**, 2749–2758.

34 H. Du, L. Jiao, Q. Wang, Q. Huan, L. Guo, Y. Si, Y. Wang and H. Yuan, *CrystEngComm*, 2013, **15**, 6101–6109.

35 T. Brezesinski, B. Smarsly, K. Iimura, D. Grosso, C. Boissière, H. Amenitsch, M. Antonietti and C. Sanchez, *Small*, 2005, **1**, 889–898.

36 X. Xia and B. D. Vogt, *Langmuir*, 2020, **36**, 1288–1297.

37 H.-J. Butt and M. Jaschke, *Nanotechnology*, 1995, **6**, 1–7.

38 N. Fairley, V. Fernandez, M. Richard-Plouet, C. Guillot-Deudon, J. Walton, E. Smith, D. Flahaut, M. Greiner, M. Biesinger, S. Tougaard, D. Morgan and J. Baltrusaitis, *Appl. Surf. Sci. Adv.*, 2021, **5**, 100112.

39 C. C. L. McCrory, S. Jung, J. C. Peters and T. F. Jaramillo, *J. Am. Chem. Soc.*, 2013, **135**, 16977–16987.

40 H. K. Christenson, J. Fang and J. N. Israelachvili, *Phys. Rev. B: Condens. Matter Mater. Phys.*, 1989, **39**, 11750–11754.

41 T. Huang, W. Huang, C. Zhou, Y. Situ and H. Huang, *Surf. Coat. Technol.*, 2012, **213**, 126–132.

42 W. Xing, F. Li, Z. Yan and G. Q. Lu, *J. Power Sources*, 2004, **134**, 324–330.

43 M. Zheng, J. Cao, S. Liao, J. Liu, H. Chen, Y. Zhao, W. Dai, G. Ji, J. Cao and J. Tao, *J. Phys. Chem. C*, 2009, **113**, 3887–3894.

44 M. Einert, T. Weller, T. Leichtweiß, B. M. Smarsly and R. Marschall, *ChemPhotoChem*, 2017, **1**, 326–340.

45 A. Amirzhanova, N. Akmanşen, I. Karakaya and Ö. Dag, *ACS Appl. Energy Mater.*, 2021, **4**, 2769–2785.

46 E. Ortel, T. Reier, P. Strasser and R. Kraehnert, *Chem. Mater.*, 2011, **23**, 3201–3209.

47 M. Bernicke, E. Ortel, T. Reier, A. Bergmann, J. Ferreira de Araujo, P. Strasser and R. Kraehnert, *ChemSusChem*, 2015, **8**, 1908–1915.

48 S. Anantharaj and S. Noda, *Small*, 2020, **16**, 1905779.

49 W. Liu, H. Liu, L. Dang, H. Zhang, X. Wu, B. Yang, Z. Li, X. Zhang, L. Lei and S. Jin, *Adv. Funct. Mater.*, 2017, **27**, 1603904.

50 T. E. Quickel, V. H. Le, T. Brezesinski and S. H. Tolbert, *Nano Lett.*, 2010, **10**, 2982–2988.

51 M. Einert, A. Waheed, D. C. Moritz, S. Lauterbach, A. Kundmann, S. Daemi, H. Schlaad, F. E. Osterloh and J. P. Hofmann, *Chem. – Eur. J.*, 2023, **29**, e202300277.

52 T. von Graberg, P. Hartmann, A. Rein, S. Gross, B. Seelandt, C. Röger, R. Zieba, A. Traut, M. Wark, J. Janek and B. M. Smarsly, *Sci. Technol. Adv. Mater.*, 2011, **12**, 025005.

53 M. Einert, A. Waheed, S. Lauterbach, M. Mellin, M. Rohnke, L. Q. Wagner, J. Gallenberger, C. Tian, B. M. Smarsly, W. Jaegermann, F. Hess, H. Schlaad and J. P. Hofmann, *Small*, 2023, **19**, 2205412.

54 J. van Elp, J. L. Wieland, H. Eskes, P. Kuiper, G. A. Sawatzky, F. M. F. de Groot and T. S. Turner, *Phys. Rev. B: Condens. Matter Mater. Phys.*, 1991, **44**, 6090–6103.

55 W. L. Roth, *J. Phys. Chem. Solids*, 1964, **25**, 1–10.

56 D. L. Rousseau, R. P. Bauman and S. P. S. Porto, *J. Raman Spectrosc.*, 1981, **10**, 253–290.

57 V. G. Hadjiev, M. N. Iliev and I. V. Vergilov, *J. Phys. C Solid State Phys.*, 1988, **21**, L199–L201.

58 C. Lohaus, J. Morasch, J. Brötz, A. Klein and W. Jaegermann, *J. Phys. Appl. Phys.*, 2016, **49**, 155306.

59 Z. Xiao, Y.-C. Huang, C.-L. Dong, C. Xie, Z. Liu, S. Du, W. Chen, D. Yan, L. Tao, Z. Shu, G. Zhang, H. Duan, Y. Wang, Y. Zou, R. Chen and S. Wang, *J. Am. Chem. Soc.*, 2020, **142**, 12087–12095.

60 J. Bao, X. Zhang, B. Fan, J. Zhang, M. Zhou, W. Yang, X. Hu, H. Wang, B. Pan and Y. Xie, *Angew. Chem.*, 2015, **127**, 7507–7512.

61 X. Yan, L. Tian, M. He and X. Chen, *Nano Lett.*, 2015, **15**, 6015–6021.

62 M. C. Biesinger, B. P. Payne, A. P. Grosvenor, L. W. M. Lau, A. R. Gerson and R. St. C. Smart, *Appl. Surf. Sci.*, 2011, **257**, 2717–2730.

63 S. A. Makhlouf, Z. H. Bakr, K. I. Aly and M. S. Moustafa, *Superlattices Microstruct.*, 2013, **64**, 107–117.

64 C.-S. Cheng, M. Serizawa, H. Sakata and T. Hirayama, *Mater. Chem. Phys.*, 1998, **53**, 225–230.

65 D. Barreca, C. Massignan, S. Daolio, M. Fabrizio, C. Piccirillo, L. Armelao and E. Tondello, *Chem. Mater.*, 2001, **13**, 588–593.

66 L. Qiao, H. Y. Xiao, H. M. Meyer, J. N. Sun, C. M. Rouleau, A. A. Puretzky, D. B. Geohegan, I. N. Ivanov, M. Yoon, W. J. Weber and M. D. Biegalski, *J. Mater. Chem. C*, 2013, **1**, 4628–4633.

67 M. Einert, P. Hartmann, B. Smarsly and T. Brezesinski, *Sci. Rep.*, 2021, **11**, 17687.

68 M. Schröder, S. Sallard, M. Böhm, M. Einert, C. Suchomski, B. M. Smarsly, S. Mutisya and M. F. Bertino, *Small*, 2014, **10**, 1566–1574.

69 M. Hamdani, R. N. Singh and P. Chartier, *Int. J. Electrochem. Sci.*, 2010, **5**, 556–577.

70 Y. Surendranath, M. W. Kanan and D. G. Nocera, *J. Am. Chem. Soc.*, 2010, **132**, 16501–16509.

71 B. Sidhureddy, J. S. Dondapati and A. Chen, *Chem. Commun.*, 2019, **55**, 3626–3629.

72 X. Deng and H. Tüysüz, *ACS Catal.*, 2014, **4**, 3701–3714.

73 Y. J. Sa, K. Kwon, J. Y. Cheon, F. Kleitz and S. H. Joo, *J. Mater. Chem. A*, 2013, **1**, 9992.

74 Y. Zhou, S. Sun, C. Wei, Y. Sun, P. Xi, Z. Feng and Z. J. Xu, *Adv. Mater.*, 2019, **31**, 1902509.

75 R.-N. Singh, M. Hamdani, J.-F. Koenig, G. Poillerat, J. L. Gautier and P. Chartier, *J. Appl. Electrochem.*, 1990, **20**, 442–446.

76 N. Weidler, S. Paulus, J. Schuch, J. Klett, S. Hoch, P. Stenner, A. Maljusch, J. Brötz, C. Wittich, B. Kaiser and W. Jaegermann, *Phys. Chem. Chem. Phys.*, 2016, **18**, 10708–10718.

77 F. P. Lohmann-Richters, B. Abel and Á. Varga, *J. Mater. Chem. A*, 2018, **6**, 2700–2707.

78 P. Connor, J. Schuch, B. Kaiser and W. Jaegermann, *Z. Phys. Chem.*, 2020, **234**, 979–994.

79 L. Zhang, J. Zhu, X. Li, S. Mu, F. Verpoort, J. Xue, Z. Kou and J. Wang, *J. Interdiscip. Math.*, 2022, **1**, 51–87.

80 R. Paul, Q. Zhai, A. K. Roy and L. Dai, *J. Interdiscip. Math.*, 2022, **1**, 28–50.